Supplementary Information for

High-order diffraction for optical superfocusing

Jun He[1,#], Hong Liu[2,#], Dong Zhao[1,#], Jodhbir S. Mehta[3], Cheng-Wei Qiu[4], Fangwen Sun[1], Jinghua Teng[2,*], Kun Huang[1,*]

[1]Department of Optics and Optical Engineering, University of Science and Technology of China, Hefei, Anhui 230026, China
[2]Institute of Materials Research and Engineering, Agency for Science Technology and Research (A*STAR), 2 Fusionopolis Way, #08-03, Innovis, Singapore 138634, Singapore
[3]Tissue Engineering and Cell Therapy Group, Singapore Eye Research Institute, Singapore
[4]Department of Electrical and Computer Engineering, National University of Singapore, 4 Engineering Drive 3, Singapore 117576, Singapore

[#] *J. H.*, *H. L.* and D. Z. contributed equally to this work.
[*]Corresponding authors: J. T. (jh-teng@imre.a-star.edu.sg) or K. H. (huangk17@ustc.edu.cn)

Table of contents

Supplementary Section 1. On-axis intensity of light diffracted from an axisymmetric zone

To calculate the on-axis intensity of optical diffraction from a zone, we employ Rayleigh-Sommerfeld diffraction by assuming that the incident light in this zone has an electric field $E(x_0, y_0)$, where x_0 and y_0 are the coordinates at the plane of the zone. If the zone has the outermost and inner radii of r_n and r_{n-1}, we have the electric field of its diffracted light at the position (x, y, z)

$$E(x,y,z) = -\frac{1}{2\pi}\iint_{-\infty}^{\infty} E(x_0,y_0)\cdot\frac{\partial}{\partial z}\left(\frac{e^{ikR}}{R}\right)dx_0dy_0 \qquad (S1)$$

where $R = \sqrt{(x-x_0)^2 + (y-y_0)^2 + z^2}$, k=2π/λ, λ is the wavelength of the incident light, and uniform illumination with $E(x_0,y_0)=1$ is used here. By setting $x=y=0$ in Eq. (S1), we can obtain the on-axis electric field in polar coordinates

$$\begin{aligned} E(0,0,z) &= \frac{\partial}{\partial z}\left(-\frac{1}{2\pi}\int_0^{2\pi}d\varphi\int_{r_{n-1}}^{r_n}\frac{e^{ikR}}{R}rdr\right) \\ &= -\frac{\partial}{\partial z}\left(\int_{r_{n-1}}^{r_n}\frac{e^{ikR}}{R}rdr\right) \\ &= -\frac{\partial}{\partial z}\left(\int_{R_{n-1}}^{R_n}\frac{e^{ikR}}{R}RdR\right) \\ &= -\frac{1}{ik}\cdot\frac{\partial}{\partial z}\left(e^{ikR_n} - e^{ikR_{n-1}}\right) \\ &= e^{ikR_{n-1}}\frac{z}{R_{n-1}} - e^{ikR_n}\frac{z}{R_n}, \end{aligned} \qquad (S2)$$

where $r^2=x_0^2+y_0^2$, $R_n = \sqrt{r_n^2 + z^2}$, and $R_{n-1} = \sqrt{r_{n-1}^2 + z^2}$. Thus, we have the on-axis intensity

$$I(0,0,z) = \frac{z^2}{R_n^2} + \frac{z^2}{R_{n-1}^2} - \frac{z^2}{R_nR_{n-1}}2\cos(k\Delta R), \qquad (S3)$$

where $\Delta R=R_n-R_{n-1}$. When $z=f$, we can obtain the on-axis intensity at the designed focus, which has been used to construct Fig. 1c in the main text. The item $\cos(k\Delta R)$ in Eq. (S3) is valued between -1 (i.e., $k\Delta R=(2M+1)\pi$) and 1 (i.e., $k\Delta R=2M\pi$), which are related to the constructive and destructive interferences. By using destructive interference, we can judge the boundary of each diffraction order from the zone.

We must emphasize that, when destructive interference occurs (i.e., $\cos(k\Delta R)=1$), the on-axis intensity $I(0, 0, z)=z^2(1/R_n - 1/R_{n-1})^2$ is greater than zero at a finite propagation distance z because $R_n \neq R_{n-1}$ for a realistic zone. However, when $z=\infty$, it leads to $z=R_n$ and $z=R_{n-1}$, which indicates that I(0,0, z)=0 with a physically reasonable solution.

Supplementary Section 2. Light intensity profiles for diffractes from a zone

In Fig. 1c of the main text, we present the on-axis intensity profiles at the focal plane of the zones with different widths and outermost radii. To visualize the diffraction field of a zone, we present two special cases: A ($sin\alpha = 0.45, \Delta r = 4.69\lambda$) and B ($sin\alpha = 0.5, \Delta r = 7.6\lambda$), which are related to destructive and constructive interferences, respectively. Both diffraction patterns are provided in Supplementary Fig. 1. For the zone with its parameters located at point A, the on-axis intensity is minimal at z=~30 μm (λ=405 nm); see Supplementary Fig. 1a. In contrast, the on-axis light has a peak at z=~30 μm, which is attributed to the 3rd order diffraction light for case B.

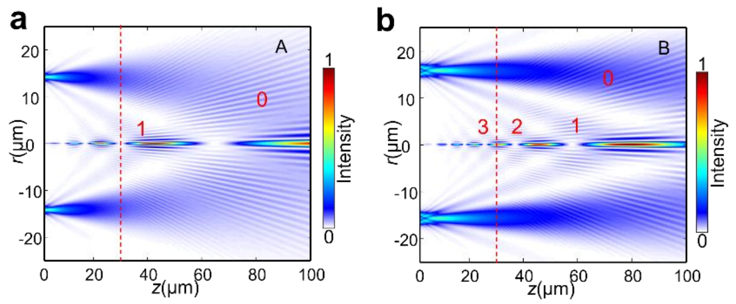

Supplementary Figure 1. Diffraction field of rings located at points A (a) and B (b) in the map of diffraction order (see Fig.1c in the main text). The red dashed line indicates the position z=30 μm. The zone located at point A has the width of 4.69λ and $sin\alpha = 0.45$, while the zone located at point B has the width of 7.6λ and $sin\alpha = 0.5$. The wavelength λ is 405 nm and the focal length is f=75λ≈30 μm.

Supplementary Section 3. Structural dimensions of the designed high-order lenses (HOLs)

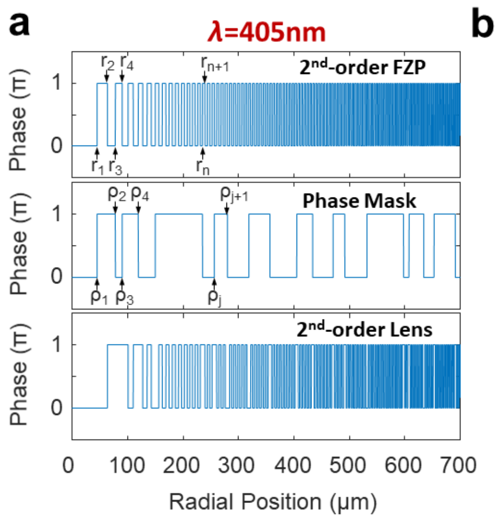

b

j	ρj (μm)	j	ρj (μm)	j	ρj (μm)
1	45	13	470.8	25	985.5
2	78	14	491.8	26	988.4
3	90.1	15	531.9	27	1061.9
4	119.3	16	597.8	28	1084.1
5	149.7	17	607.6	29	1186.6
6	235.4	18	634.4	30	1222.2
7	256.6	19	653.1	31	1337.8
8	280.1	20	691.3	32	1350.5
9	318.9	21	753.5	33	2060
10	356.8	22	794.9		
11	405.2	23	856.9		
12	434	24	881.6		

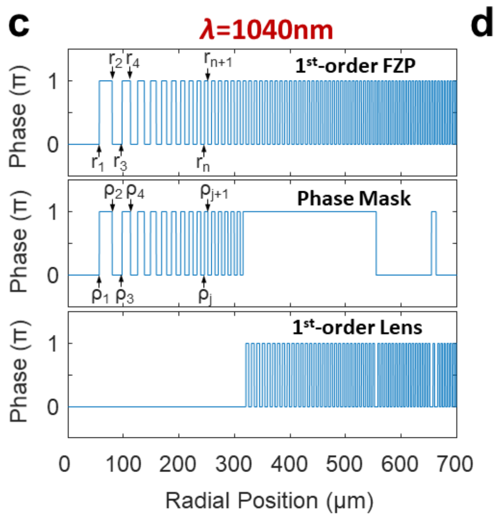

d

j	ρj (μm)	j	ρj (μm)	j	ρj (μm)
1	55.9	13	202.4	25	282
2	79.1	14	210.1	26	287.7
3	96.9	15	217.6	27	293.3
4	111.9	16	224.8	28	298.8
5	125.1	17	231.8	29	304.2
6	137.1	18	238.6	30	309.5
7	148.2	19	245.3	31	314.7
8	158.5	20	251.7	32	554.7
9	168.2	21	258.1	33	654.2
10	177.3	22	264.2	34	622.7
11	186	23	270.3	35	2056.8
12	194.4	24	276.2		

Supplementary Figure 2. Structural parameters of our proposed 2nd-order lens (**a-b**) at λ=405 nm and 1st-order lens (**c-d**) at λ=1040 nm. The phase profiles in **(a)** and **(c)** are provided in detail by addressing the relative high-order FZP, the phase mask and the combined high-order lens. Because the structural parameters of the related high-order FZP can be obtained directly by using our proposed analytical formula Eq. (2) in the main text, we need to provide only the structural dimensions of the phase masks, which are provided in (b) for λ=405 nm and (d) for λ=1040 nm.

In this work, we have developed two kinds of high-order lenses with binary phases for demonstration via confocal imaging and lithography. In the first demonstration of confocal imaging, the 2^{nd}-order lens with a focal length of 1 mm and a numerical aperture of 0.9 is designed at a wavelength of 405 nm. With these parameters M=2, f=1 mm and NA=0.9, we can derive the dimension of the relative 2^{nd}-order FZP, which has the smallest feature size of 1.1 μm for low-cost fabrication. The additional phase mask is optimized by using particle swarm algorithms to suppress the focal size down to the subdiffraction-limit scale, thus yielding the designed radii of the phase mask (see Supplementary Fig. 2b). By combining the phase profiles of the 2^{nd}-order FZP and the optimized mask, we can obtain the final phase profiles of the 2^{nd}-order lens, as shown in the bottom row in Supplementary Fig. 2a. It is important to emphasize that the plotted coordinates are limited to r=700 μm for better observation of the structural details. One can see more details by drawing the phase profiles with our provided parameters. This 2^{nd}-order lens is used for scanning confocal imaging with subdiffraction-limit resolution.

The second lens is designed at a wavelength of 1040 nm for laser-ablation lithography. The entire design and fabrication process are the same as those for the 2^{nd}-order lens at the wavelength of 405 nm. The 1^{st}-order lens at λ=1040 nm has a focal length of 1 mm, a numerical aperture of 0.9, and a diameter of ~4 mm. Its radial phase profiles from r=0 to r=700 nm are provided in Supplementary Fig. 2c. The detailed parameters of the designed phase mask are presented in Supplementary Fig. 2d.

Supplementary Section 4. Characterizing the focusing properties of high-order lenses (HOLs)

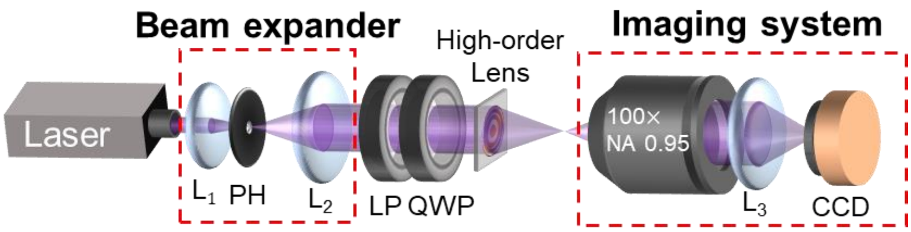

Supplementary Figure 3. Experimental setup for characterizing the focusing capability of the PDL. The beam expander consists of lenses L_1 and L_2 (with focal lengths of 25.4 mm and 300 mm, respectively) and a 25 μm-diameter pinhole. The imaging system consists of a 100× objective with a 0.95 NA, a lens L_3 (with a focal length of 400 mm) and a CCD camera. LP: linear polarizer. QWP: quarter-wave plate.

To characterize the focusing capability of the high-order lens, we utilize the experimental setup depicted in Supplementary Fig. 3. The beam from a laser is reshaped by using a beam expander that comprises lenses L_1 and L_2, as well as a 25 μm-diameter pinhole, resulting in a fundamental Gaussian beam with a diameter of approximately 1 mm. Circularly polarized illumination is generated by employing a linear polarizer and a quarter-wave plate to achieve a highly axisymmetric focal spot. Subsequently, the subdiffraction-limit focal spot generated by the high-order lens is projected onto a CCD camera by using an imaging system composed of a 100× objective lens with a numerical aperture of 0.95 and a lens L_3.

The above experimental setup is available for characterizing the focusing properties of both 2^{nd}-order lenses at λ=405 nm and 1^{st}-order lens at λ=1040 nm. The only difference is the laser source.

A 405 nm continuous-wave laser is used for the 2nd-order lens, while a femtosecond pulse laser with a center wavelength of 1040 nm and a spectral width of 10 nm is used for the case of 1st-order lens.

Supplementary Section 5. Images simulated by using different microscopies

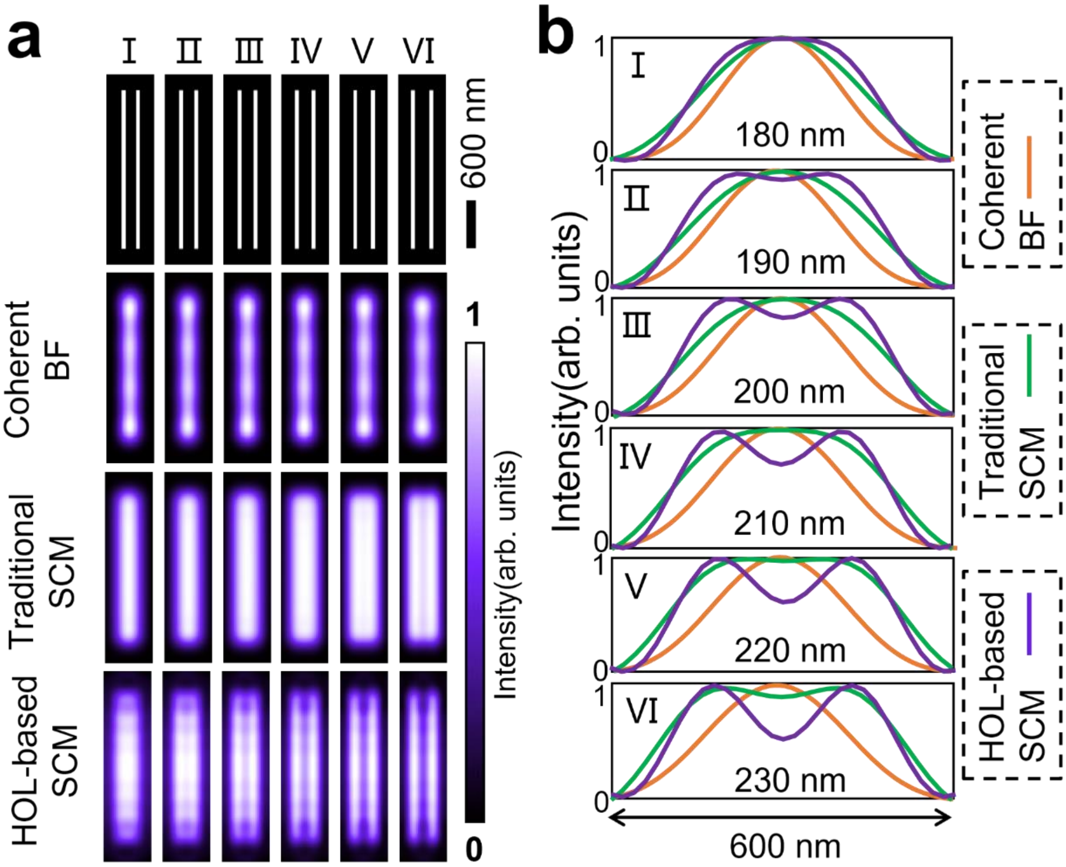

Supplementary Figure 4. Simulated images of double slits with different CTC distances. **(a)** Sketch of double slits and their simulated images obtained by using a coherent bright field (BF) microscope, traditional SCM and HOL-based SCM. The lengths and widths of the slits are 2 μm and 50 nm, respectively. The CTC distances of the double slits are 180 nm (I), 190 nm (II), 200 nm (III), 210 nm (IV), 220 nm (V) and 230 nm (VI). Image size: 2.4 μm×0.6 μm. Scale bars: 600 nm. **(b)** Line-scanning profiles of these simulated images obtained by addressing the CTC distances of double slits.

We employ coherent imaging theory to provide a numerical simulation of images that are obtained through different microscopies. In these simulations, we use double slits with a fixed width of 50 nm and vary the center-to-center (CTC) distance to maintain consistency with our experimental cases. To simulate images of double slits with a coherent bright-field microscope, we perform convolutions between the objects and an Airy spot of $\frac{J_1(krNA)}{krNA}$, where *NA* is 0.9. Similarly, we conduct the simulations of traditional scanning confocal microscopy (SCM) and HOL-based SCM by using the principles of SCM as described in reference [1]. In both simulations, the point spread functions (PSFs) of the condenser lens and the collection lens in traditional SCM are represented as the Airy spots with an amplitude of $\frac{J_1(krNA)}{krNA}$. In the simulation for traditional SCM, the condenser lens is characterized by an objective lens with a numerical aperture (*NA*) of 0.9, and the collection lens with an *NA* of 0.95. On the other hand, in the simulation of our HOL-based SCM, the PSF of the condenser lens is the simulated electric field of our HOLs, while the PSF of a collector lens is represented as an Airy spot $\frac{J_1(krNA)}{krNA}$ with *NA* of 0.95.

Supplementary Figure 4 shows images simulated by using different microscopies. Like our experimental findings, coherent bright-field microscopy fails to resolve any double slits, indicating its limited resolving power. On the other hand, a traditional SCM utilizing a refraction-based objective can resolve only double slits with a center-to-center (CTC) distance of 230 nm, which agrees with the results in Fig. 3 of the main text. In contrast, our HOL-based SCM can resolve double slits with a CTC distance of 190 nm.

Supplementary Section 6. Focusing properties of the 1st-order lens for laser-ablation lithography

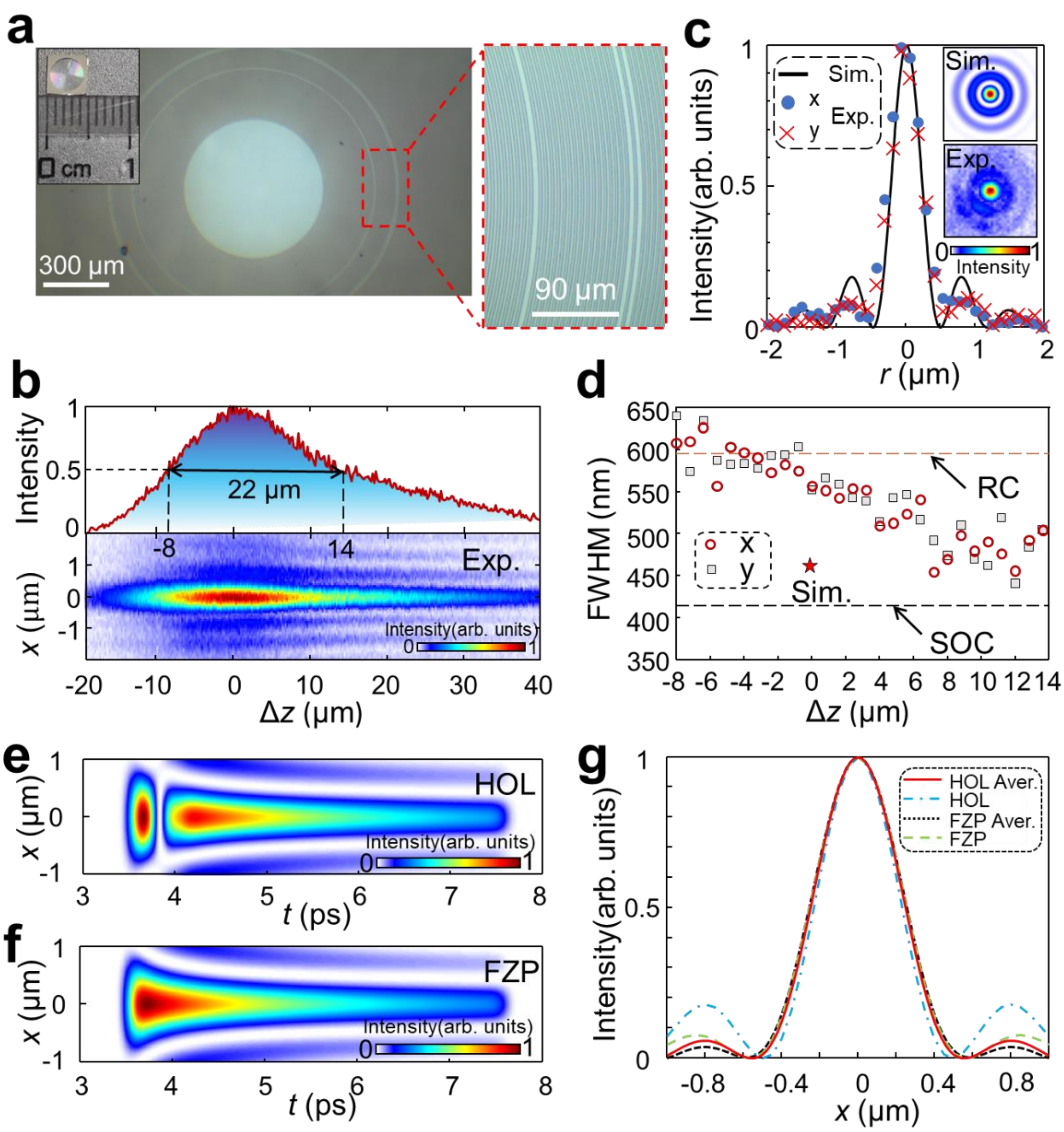

Supplementary Figure 5. 1st-order lens for laser-ablation lithography. (a) Optical microscope image of the 1st-order lens. Insert: a photo of the lens. A magnified image as labelled with a red dashed box is presented in the right panel. **(b)** Measured intensity profiles near the focal region from $\Delta z = -20\ \mu\text{m}$ to $\Delta z = 40\ \mu\text{m}$, where $\Delta z = z - f$ and $f = 1\ \text{mm}$. The incident light is a femtosecond laser with its central wavelength of 1040 nm and spectral width of 10 nm. The on-axis intensity is presented in the upper panel, which indicates that the longitudinal DOF of the on-axis intensity is $22\ \mu m$. **(c)** Experimental and simulated line-scanning intensity profiles at the focal plane *z*=*f*. Insert: simulated and experimental intensity profiles in two dimensions. **(d)** Measured lateral FWHM near the focal region. RC: Rayleigh criterion ($0.515\lambda/NA$), SOC: Superoscillation criterion ($0.358\lambda/NA$). The red star shows the simulated FWHM of spot at the focal plane. **(e-f)** Simulated temporal intensity profiles of the 1st-order lens **(e)** and its corresponding 1st-order FZP **(f)** when illuminated by a femtosecond laser with its central wavelength of 1040 nm and a spectral width of 10 nm. **(g)** Line-scanning intensity profiles at the focal planes of HOL and FZP. The time average of the focal spots are provided to show the increment of the spot under the illumination of the ultrashort pulse.

We design a 1st-order lens with a working wavelength of λ=1040 nm and a focal length of *f*=1 mm, utilizing a high-order FZP with *M*=1. This 1st-order FZP consists of 825 zones (i.e., *N* = 825), leading to an approximate diameter of ~4 mm. The optimized phase mask consists of 35 rings, and the parameters are shown in Supplementary Fig. 2d. Consequently, the 1st-order lens possesses a total of 791 concentric zones with a minimum size of 1.7 μm and a NA of 0.9, where its images of the fabricated 1st-order lens is illustrated in Supplementary Fig. 5a. Since this 1st-order lens is designed for laser-ablation lithography, we measure the diffraction field near the focus of the 1st-order lens when illuminated with circularly polarized femtosecond pulse light, see the measurement setup in Supplementary Fig. 3. The femtosecond laser has a central wavelength of 1040 nm and a spectral width of 10 nm (FWHM). The objective with *NA* of 0.95 is utilized to make sure that the light for focusing diffracted from this 1st-order lens is collected. The on-axis line-scanning intensity profile shown in the upper panel of Supplementary Fig. 5b indicates that the experimental longitudinal depth of focus (DOF) can reach 20 μm. The simulated and experimental line-scanning intensity profiles at the focal plane are shown in Supplementary Fig. 5c, which indicates that the experimental lateral FWHM of 550 nm (0.53λ) is larger than the designed value of 450 nm (0.44λ). Nevertheless, this focal spot size is still smaller than RC (Rayleigh criterion: 0.57λ, calculated by $0.515\lambda/NA$ at *NA*=0.9) and larger than SOC (Superoscillation criterion: 0.4λ, calculated by $0.358\lambda/NA$ at *NA*=0.9), which is taken as the super-critical focusing. The lateral FWHM of a significant portion of the optical needles falls within the range of RC and SOC, although it is larger than the designed value labelled by red star (as shown in Supplementary Fig. 5d).

The enlargement of the measured focal spot may be caused by the dispersion of the 1st-order lens under the illumination of a femtosecond pulse. To investigate the temporal focusing of this 1st-order lens, we firstly utilize the Rayleigh-Sommerfeld diffraction theory to obtain the diffraction field at a single temporal frequency w:

$$E(x, y, z, w) = -\frac{1}{2\pi}\iint_{-\infty}^{\infty} E(x_0, y_0, w) \cdot \frac{e^{ikR}}{R^2}\left(ik - \frac{1}{R}\right) \cdot z\, dx_0 dy_0, \qquad (S4)$$

where $R = \sqrt{(x - x_0)^2 + (y - y_0)^2 + z^2}$, x_0 and y_0 are the coordinates of the incident plane, *x* and *y* are the spatial coordinates at the output plane, and the wavevector $k = w/c$, *c* is the speed of light. When ignoring the inherent dispersion in the femtosecond pulse and the small dispersion of materials, the electric field in incident plane can be written as $E(x_0, y_0, w) = U(x_0, y_0)A(w)$, which means that the lateral beam profiles at the different wavelengths have no significant variation.

Thus, in our simulation, the function $U(x_0, y_0)$ can be used as the transmissive function of our 1st-order lens. The frequency-dependent spectral function $A(w)$ has a Gaussian shape of $A(w) = e^{-(\frac{w-w_0}{\Delta w})^2}$, which is basically the same with most line-shapes of the femtosecond lasers. To simulate the femtosecond pulse used in this work, the carrier frequency w_0 is approximately $1.8125\ \mu m/fs$ and spectral width of Δw is approximately $0.0167\ \mu m/fs$. Then, the temporal profile of focusing at the output plane can be achieved by using Fourier transform:

$$E(x, y, z, t) = \int_{-\infty}^{\infty} E(x, y, z, w) \cdot e^{-iwt} dw . \qquad (S5)$$

According to Eqs. S4 and S5, the temporal intensity profiles of the 1st-order lens at focal plane are presented on Supplementary Fig. 5e. The light emitted from the center of 1st-order lens first reaches the focal point, but the light diffracted from the edge of 1st-order lens reaches the focal point later. Therefore, the focal intensity appears at ~3.3 ps and ends at ~7.5 ps. The temporal intensity profile of high-order FZP having the same *NA* and focal length with the 1-order lens is also presented in Supplementary Fig. 5f. Compared with the 1st-order lens, the temporal intensity of FZP is continuous without any gap. Because the focal intensity of the 1st-order lens (Supplementary Fig. 3c) is measured by a traditional CCD with an extremely lower response speed than the time scale of several picoseconds, the measured intensity is the time average of the temporal pulse, i.e.,:

$$I_{measured} = \frac{1}{T} \int_0^T I(t) dt . \qquad (S6)$$

Therefore, the time average of line-scanning intensity is shown in Supplementary Fig. 5g. Compared with the line-scanning focal intensity under the CW laser illumination, the time average of line-scanning intensity profile with the incident femtosecond laser has a larger FWHM.

Supplementary Section 7. Laser-ablation lithography with a high-order lens

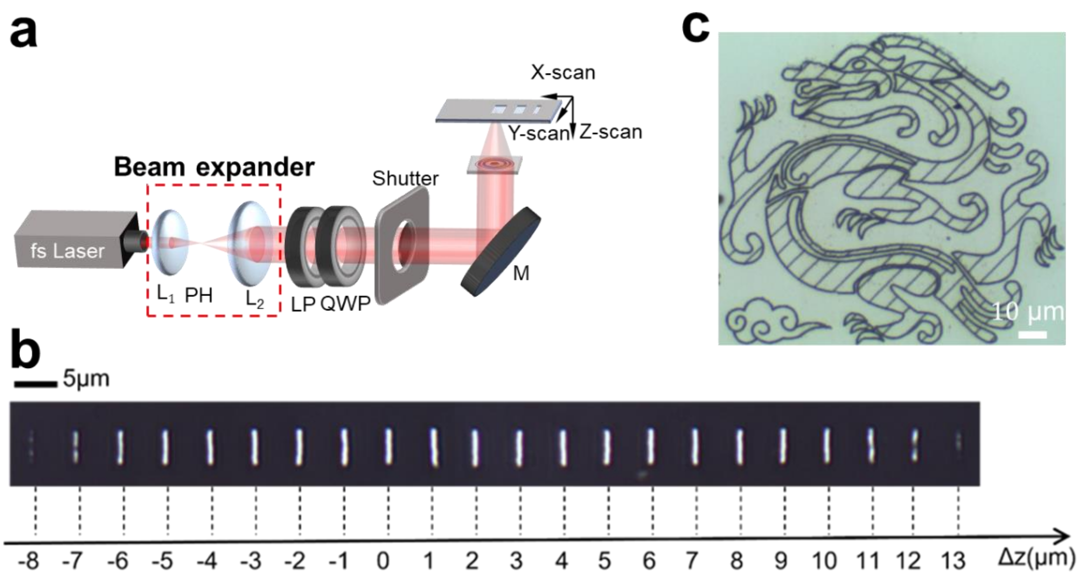

Supplementary Figure 6. (a) Experimental setup for laser-ablation lithography with a high-order lens. The beam expander consists of lenses L_1 and L_2 (with the focal lengths of 25.4 mm and 100 mm, respectively). LP: linear polarizer, QWP: quarter-wave plate, PH: pinhole, M: mirror. **(b)** Transmissive optical microscope images of single slits fabricated by using the different parts of optical needle. The out-of-focus distance Δz=*z*-*f* ranges from Δz=-8 μm to Δz=13 μm. The exposure time for all the slits is 200 ms. **(c)** Fabricated patterns.

To develop lithography with the 1st-order lens, we employ a self-built setup as illustrated in Supplementary Fig. 6a. The incident femtosecond pulse has a center wavelength of 1040 nm and a spectral width of 10 nm. A beam expander, consisting of two lenses, is used to expand the femtosecond pulse to match the dimensions of the lens. By combining a linear polarizer and a quarter-wave plate, a circularly polarized light is generated to experimentally obtain the circularly symmetric focal spot. A shutter is employed to control the exposure time of the sample. The sample is mounted on a 3D piezo stage, and both the shutter and the piezo stage are controlled by a single computer simultaneously. The fabrication details are provided in the Methods of the main text.

In laser-ablation-based lithography, the uniformity of optical needle is important to obtain well-behaved patterning. To evaluate the uniformity of the needle, two parameters, including longitudinal intensity distribution and the lateral beam size, are used here. For the longitudinal intensity distribution, the measured results in Supplementary Fig. 5b show slowly varied intensity with a peak at Δz=0. Because the longitudinal intensity is not uniform, only the above-threshold parts of needle can be used to fabricate the samples in lithography. On the other hand, the patterning resolution is also related with the second parameter, i.e., the lateral beam size, which is measured and shown in Supplementary Fig. 5d. The measured beam size shows a slowly decreasing tendency at the above-threshold region from Δz=-8 μm to Δz=14 μm. After comparing the line widths (Fig. 4c in the main text) of the fabricated lines, we find that the widths of the fabricated lines have the similar tendency to that of the longitudinal intensity distribution. It means that the longitudinal intensity above the threshold dominates in the fabrication when the lateral beam size has no significant variation. Beyond these issues, the mechanical vibration of optical system will influence the shape of the fabricated lines. To show it, we provide the transmissive optical microscope images of these slits in Supplementary Fig. 6b, which signifies that some of the slits are not straight due to mechanical vibration.

Supplementary Figures 6c presents the fabricated dragon patterns. The result shows the ability of our proposed lithography to fabricate various optical elements for a wide range of applications.

Supplementary Section 8. Experimental characterization of the diffraction field of fork gratings

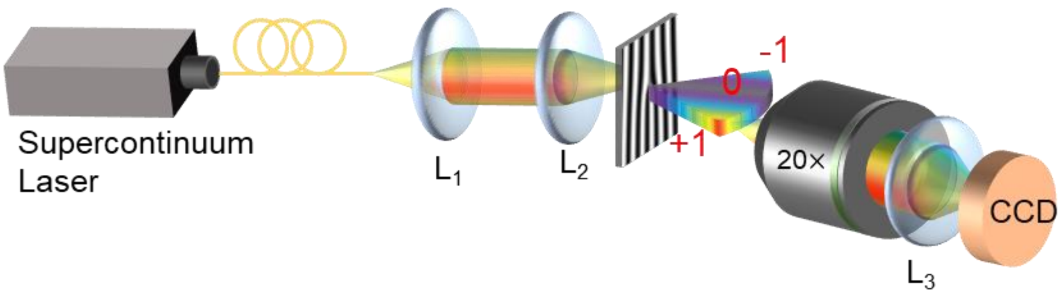

Supplementary Figure 7. Experimental setup for characterizing the diffraction field of fork grating. Lens L_1 is a collimating lens with a focal length of 25.4 mm. Lens L_2 is a 50 × objective lens for weak focusing. The imaging system consists of a 20× objective lens, a tube lens L_3 (with a focal length of 200 mm) and a CCD camera.

The setup depicted in Supplementary Figure 7 is utilized to measure the diffraction field of the fork grating fabricated by using our HOL-based laser-ablation lithography. Lens L_1 is used to collimate the incident broadband light. Due to the low diffraction efficiency and the small size of fork grating, a 50× objective lens is employed as lens L_2 to weakly focus on the forked grating. To detect the +1 (or -1) order diffraction light at the same frame, we rotate the imaging system, which consists of a 20× objective, a tube lens with a 200 mm focal length, and a CCD camera, in the corresponding direction. The resulting donut-shaped intensity at first-order diffraction from the fork grating is presented in Fig. 5 of the main text.

Supplementary Section 9. Characterizing the diffraction field from the "USTC" letters

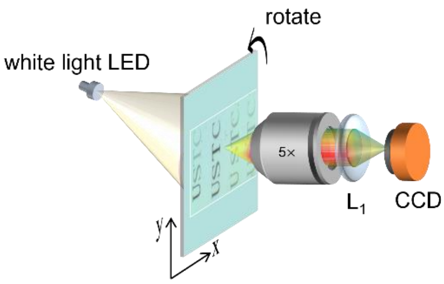

Supplementary Figure 8. Setup for characterizing the diffraction field of "USTC" letters. The imaging system consists of a 5× objective lens, a tube lens L_1 (with a focal length of 100 mm) and a CCD camera.

To obtain multi-color 1st-order diffraction, a white-light LED is used to illuminate the sample obliquely, as shown in Supplementary Fig. 8. Because each character is too small for direct observation by human eyes, an imaging system consisting of a 5× objective lens, a tube lens L_1 (with a focal length of 100 mm) and a CCD camera is employed to capture the images. To observe the directional images without rotating the imaging system, the sample is mounted on a rotator that could realize the in-plane rotation. Thus, diffraction light from the letters with an orientation along the y axis can be detected by the imaging system, which can be observed in the images in Fig. 5g and Supplementary Video 1.

Supplementary Section 10. Optical performances of planar diffractive lenses

Supplementary Table 1. A comparison of the optical performances of planar diffractive lenses

References	λ (nm)	Focal Size (λ)	NA	Ambient Medium	Focal Length (μm)	Feature Size (nm)	Ratio [a]	Efficiency [b]	Modulation type
[2]	532	0.79	0.98	oil	4	100	0.2372	0.1800%	Amplitude
[3]	532	0.32	0.99	oil	1	100	0.5882	0.5000%	Amplitude
[4]	535	1.01	0.41	air	45	500	0.9263	2.5600%	Phase
[5]	532	0.39	0.86	air	11.4	200	0.9569	0.1500%	Amplitude
[6]	532	0.39	0.86	air	11.5	200	0.9639	0.1500%	Amplitude
[7]	400	0.49	0.82	air	40	200	1.0309	20.3200%	Phase
[8]	640	0.29	0.88	oil	10.3	200	1.0811	0.6000%	Amplitude
[9]	1550	0.44	0.89	air	20	800	1.1864	2.6000%	Phase
[10]	405	0.40	0.69	air	10	200	1.2346	0.7200%	Amplitude
[11]	405	0.44	0.9	air	1000	225	1.2500	12.9400%	Phase
[12]	450	0.43	0.89	air	20	250	1.2887	1.7200%	Amplitude
[13]	633	0.50	0.83	air	63.3	470	1.4803	0.3600%	Phase

[14]	633	0.47	0.92	air	127.4	500	1.6955	0.4700%	Phase
[15]	633	0.50	0.83	air	63.3	780	2.4613	1.4500%	Phase
[16]	633	0.64	0.71	air	100	1200	2.9630	3.6000%	Phase
[17]	633	0.51	0.55	air	229	1020	3.1677	0.0900%	Amplitude
[18]	405	0.41	0.98	air	55	1200	7.2727	0.0013%	Amplitude
[19]	488	0.50	0.75	air	428	2500	10.2041	0.0100% [c]	Phase
This work	**1040**	**0.45**	**0.9**	**air**	**1000**	**1700**	**3.63**	**1.34%**	**Phase**
	405	**0.44**	**0.9**	**air**	**1000**	**1100**	**6.11**	**0.17%**	**Phase**

Notes: 1) [a] The ratio is defined as the ratio of the feature size to the focal size.

2) [b] The simulated efficiency is used here for evaluating the theoretical limitation of efficiency. To avoid any error, all the efficiency in this table is numerically calculated by using the ratio of the power in a circle with a radius 3 times the FWHM of the focal spot to the incident total power, which is consistent with the definition in the main text.

3) [c] The efficiency is calculated by using the dimensions of the reported lens in Ref. [19]. The dimensions are obtained by private communications with the corresponding authors in Ref. [19]. Our calculated efficiency of 0.01% is lower than that in Ref. [19], which overestimates the efficiency (the corrected version of Ref. [19] was available at 19 Feb. 2024).

4) The cases of metalenses are not included because their feature sizes are much smaller than the working wavelengths.

To demonstrate the advantages of our proposed high-order lenses, we provide a detailed comparison among planar diffractive lenses in several published studies[2-19], where the detailed dimensions of the lenses have been provided for checking optical performance. The Supplementary Table 1 illustrates that our proposed high-order lenses have advantages in terms of numerical aperture (*NA*), focal length, the ratio of the feature size to the focal size, compared with most of the reported lenses. It is important to point out that, although the lenses in previous reports had slightly larger ratios than our high-order lenses, our lenses have the improved efficiency, which is enhanced by 1~3 orders of magnitude compared with that of Refs. [18] and [19]. The enhancement is attributed to the HOD physics that is revealed in this work, as observed in Supplementary Fig. 9. For our proposed high-order lenses, the dimensions of most zones are chosen to obtain constructive interference because most (97.41% and 95.76% of the zones for the 2^{nd}- and 1^{st}-order lenses, respectively) dimensions are located at the maximum on-axis intensity in the maps. This means that our corresponding efficiency for optical focusing is higher than those in Refs. [18] and [19], where the selected zones are located irregularly without the optimal interference. In our proposed lenses, some discrete points located at the destructive interference are caused by the phase jump of π in the phase mask, thus making two neighboring zones emerged into one zone. Because such cases occupy only a quite small portion of the zones, it has little influence to the efficiency in our lenses. Therefore, by using the HOD physics, one can have a detailed guidance to design a diffractive lens with high efficiency and more spatial degrees of freedom for superfocusing.

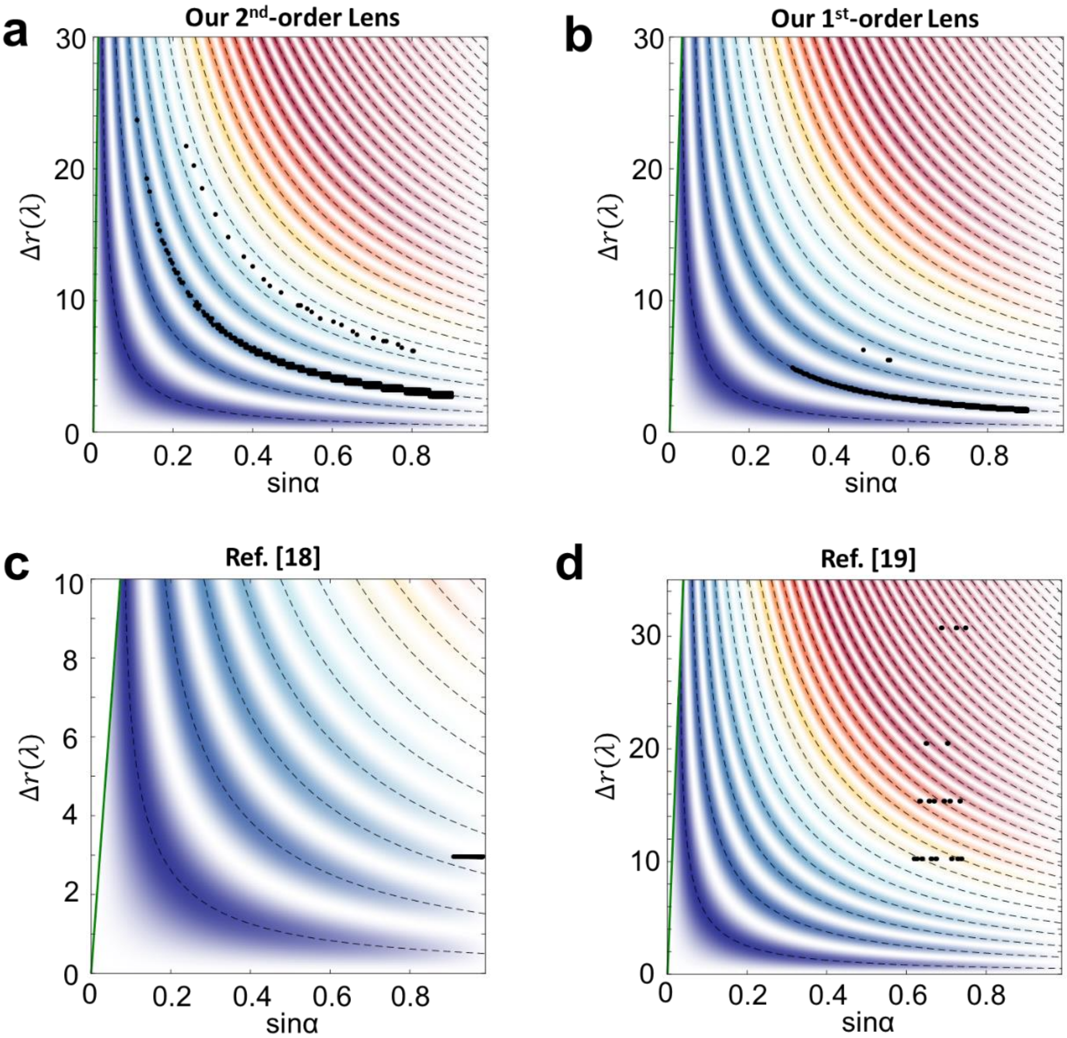

Supplementary Figure 9. Maps of diffraction orders for several reported non-subwavelength lenses and their structural dimensions. To show the HOD physics, we present the dimensions of each lens in terms of the zone width Δr and the dimensionless parameter $sin\alpha = r_n/(r_n^2+f^2)^{1/2}$, where r_n is the outermost radius of the n^{th} zone in the lens. Our 2nd-order **(a)** and 1st-order **(b)** lenses are compared with Refs. [18] **(c)** and [19] **(d)**. Because the parameter sinα depends on the focal length, these maps are plotted by addressing the own focal lengths of these lenses. The diffraction order of light diffracted from the lenses rings at each focal point is marked with black dots.

Supplementary Figure 10 shows three key features of the planar diffractive lenses, efficiency, *NA* and the ratio of the feature size to the focal size, which are listed for a better display of their performances. This comparison gives a straightforward picture about these three features, which might help the short-wavelength community to choose the suitable focusing technologies in their areas.

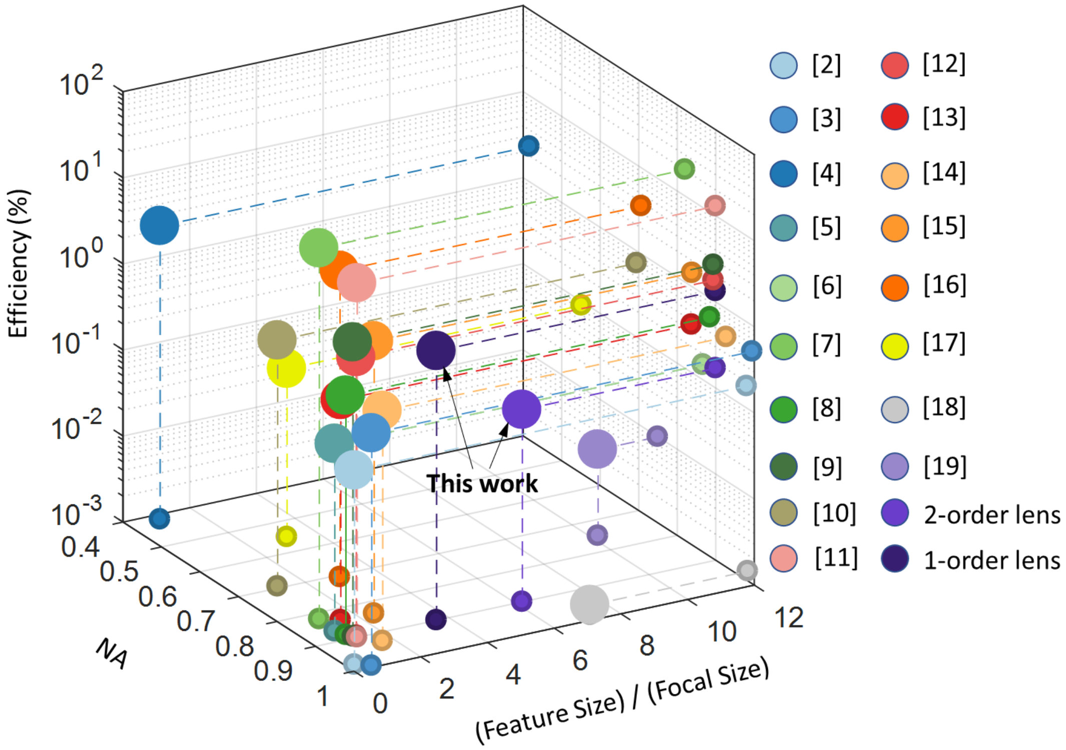

Supplementary Figure 10. Detailed comparison of the key parameters (efficiency, *NA*, and the ratio of the feature size to the focal size) of the reported lenses.

Reference

[1]. Huang, K., Qin, F., Liu, H., Ye, H., Qiu, C. W., Hong, M., Luk'yanchuk, B., & Teng, J., Planar diffractive lenses: fundamentals, functionalities, and applications, *Advanced Materials* **30**, 1704556(2018).

[2]. Diao, J., Yuan, W., Yu, Y., Zhu, Y., & Wu, Y., Controllable design of super-oscillatory planar lenses for sub-diffraction-limit optical needles, *Opt. Express* **24**, 1924(2016).

[3]. Li, M., Li, W., Li, H., Zhu, Y., & Yu, Y., Controllable design of super-oscillatory lenses with multiple sub-diffraction-limit foci, *Sci. Rep.* **7**, 1335(2017).

[4]. Qin, F., Liu, B., Zhu, L., Lei, J., Fang, W., Hu, D., Zhu, Y., Ma, W., Wang, B., & Shi, T., π-phase modulated monolayer supercritical lens, *Nat. Commun.* **12**, 32(2021).

[5]. Liu, T., Liu, J., Zhang, H., & Tan, J., Efficient optimization of super-oscillatory lens and transfer function analysis in confocal scanning microscopy, *Opt. Commun.* **319**, 31(2014).

[6]. Liu, T., Shen, T., Yang, S., & Jiang, Z., Subwavelength focusing by binary multi-annular plates: design theory and experiment, *J. Opt.* **17**, 035610(2015).

[7]. Wan, X., Shen, B., & Menon, R., Diffractive lens design for optimized focusing, *JOSA A* **31**, B27(2014).

[8]. Rogers, E. T., Lindberg, J., Roy, T., Savo, S., Chad, J. E., Dennis, M. R., & Zheludev, N. I., A super-oscillatory lens optical microscope for subwavelength imaging, *Nat. Mater.* **11**, 432(2012).

[9]. Yuan, G. H., Rogers, E. T., & Zheludev, N. I., Achromatic super-oscillatory lenses with sub-wavelength focusing, *Light: Sci. Appl.* **6**, e17036(2017).

[10]. Yuan, G., Rogers, E. T., Roy, T., Adamo, G., Shen, Z., & Zheludev, N. I., Planar super-oscillatory lens for sub-diffraction optical needles at violet wavelengths, *Sci. Rep.* **4**, 6333(2014).

[11]. He, J., Zhao, D., Liu, H., Teng, J., Qiu, C.-W., & Huang, K., An entropy-controlled objective chip for reflective confocal microscopy with subdiffraction-limit resolution, *Nat. Commun.* **14**, 5838(2023).

[12]. Wang, Z., Yuan, G., Yang, M., Chai, J., Steve Wu, Q. Y., Wang, T., Sebek, M., Wang, D., Wang, L., Wang, S.,

Chi, D., Adamo, G., Soci, C., Sun, H., Huang, K., & Teng, J., Exciton-Enabled Meta-Optics in Two-Dimensional Transition Metal Dichalcogenides, *Nano Lett.* **20**, 7964(2020).

[13]. Zhu, X., Fang, W., Lei, J., Li, Z., Xie, F., Cao, Y., Zhang, Y., Qin, F., & Li, X., Supercritical lens array in a centimeter scale patterned with maskless UV lithography, *Opt. Lett.* **45**, 1798(2020).

[14]. Yu, A.-p., Chen, G., Zhang, Z.-h., Wen, Z.-q., Dai, L.-r., Zhang, K., Jiang, S.-l., Wu, Z.-x., Li, Y.-y., & Wang, C.-t., Creation of sub-diffraction longitudinally polarized spot by focusing radially polarized light with binary phase lens, *Sci. Rep.* **6**, 38859(2016).

[15]. Fang, W., Lei, J., Zhang, P., Qin, F., Jiang, M., Zhu, X., Hu, D., Cao, Y., & Li, X., Multilevel phase supercritical lens fabricated by synergistic optical lithography, *Nanophotonics* **9**, 1469(2020).

[16]. Zhu, Z., Zheng, P., He, L., Lin, Z., Xie, X., Chen, Y., & Yu, S. *Frontiers in Optics.* FM2A. 5 (Optical Society of America).

[17]. Zhang, Z., Li, Z., Lei, J., Wu, J., Zhang, K., Wang, S., Cao, Y., Qin, F., & Li, X., Environmentally robust immersion supercritical lens with an invariable sub-diffraction-limited focal spot, *Opt. Lett.* **46**, 2296(2021).

[18]. Qin, F., Huang, K., Wu, J., Teng, J., Qiu, C.-W., & Hong, M., A Supercritical Lens Optical Label-Free Microscopy: Sub-Diffraction Resolution and Ultra-Long Working Distance, *Adv. Mater.* **29**, 1602721(2017).

[19]. Li, W., He, P., Lei, D., Fan, Y., Du, Y., Gao, B., Chu, Z., Li, L., Liu, K., An, C., Yuan, W., & Yu, Y., Super-resolution multicolor fluorescence microscopy enabled by an apochromatic super-oscillatory lens with extended depth-of-focus, *Nat. Commun.* **14**, 5107(2023).